PIER Letters

Generation of Dual-Polarized Vortex Beams in the X-Band Using Reflective Metasurface

Shuman Li, Leyuan Li, Ying Sun, Zhuopeng Wang, and Lin Shao*

College of Electronic and Information Engineering
Shandong University of Science and Technology, Qingdao, China

ABSTRACT: This paper presents a single-layer reflective metasurface for generating dual-linearly polarized orbital angular momentum (OAM) beams with mode number $l = -1$ at X-band. Phase modulation is achieved by adjusting the unit cell dimensions, which efficiently converts linearly polarized waves into vortex waves with the desired OAM mode. The proposed unit cell integrates a compact '米'-shaped inner patch with a square frame, with a compact size of $0.4\lambda_0 \times 0.4\lambda_0$, enabling independent control of both x-polarized and y-polarized waves. By varying the unit size, a broad phase shift range of 374° is achieved at 8–12 GHz. Based on phase compensation principles, the designed metasurface array successfully generates dual-polarized vortex waves at X-band. The proposed metasurface exhibits high gain, narrow beam divergence, wide bandwidth, and dual-polarization capability, demonstrating significant potential for OAM wave multiplexing in wireless communication systems.

1. INTRODUCTION

Angular momentum is one of the natural characteristics of electromagnetic waves, consisting of spin angular momentum (SAM) and orbital angular momentum (OAM) [1]. Electromagnetic waves carrying OAM are known as vortex waves, characterized by their distinctive helical wavefront phase distribution. The wavefront of a vortex beam is described by the phase factor $\exp(il\varphi)$, where φ denotes the azimuthal angle in the polar coordinate system, and l represents the number of modes, indicating that the phase variation is integer multiple of 2π [2]. Encoding and multiplexing using OAM modes can significantly enhance spectral efficiency [3]. Antennas carrying OAM constitute a key research topic in 5G technology [4] and are identified as a key antenna technology for 6G development. Recognizing this potential, vortex beams have been applied in various scenarios, such as radio propagation [3, 5], fiber transmission [6–8], and quantum communication [9, 10].

Currently, the methods for generating vortex beams include using integratable quarter-wave plates [11], spiral phase plates [10], antenna arrays [12], and metasurfaces [13, 14]. Reflective metasurfaces combine the features of reflectors and antenna arrays, which have advantages of simple structures, low costs, and easy fabrication. Previous studies have successfully generated single polarized vortex beams using metasurfaces [13–16]. Furthermore, recent advancements include a low-profile circularly polarized hybrid metasurface antenna integrating both folded reflectarray and transmitarray functionalities, enabling beam switching and OAM mode switching [17]. Additionally, a broadband continuous integer- and fractional-order multimode OAM beam generator has been realized using a metasurface [18]. However, a key limitation

of metasurfaces lies in the bandwidth constraints imposed by their microstrip elements [19]. Therefore, achieving wideband vortex beam generation with metasurfaces remains a significant challenge. Moreover, conventional metasurfaces typically support only single-polarization transmission. If multiple polarizations could be generated simultaneously, it could effectively reduce the number of antennas deployed and achieve polarization multiplexing of vortex waves.

In this paper, a reflective metasurface for generating dual-linearly polarized vortex waves at X-band is proposed. Fig. 1 shows the conceptual diagram of the reflective metasurface. The proposed unit structure consists of a '米'-shaped inner patch with a square frame. As the mode number of vortex waves increases, the overall system efficiency tends to decline, which can affect the communication capacity in practical applications. Therefore, our design adopts a relatively low-order mode $l = -1$. The generated vortex waves exhibit broadband, high gain, narrow divergence angle, and dual polarizations. To verify the feasibility of this design, a prototype metasurface with $l = -1$ is fabricated and measured. Measured results are in good agreement with the simulated ones.

2. DESIGN OF METASURFACE UNIT

The unit structure of the proposed metasurface is shown in Fig. 2. Its period p is 12 mm ($0.4\lambda_0$), where λ_0 is the wavelength at central frequency 10 GHz. The top layer comprises a '米'-shaped inner patch with a square frame. The structure exhibits mirror symmetry in both horizontal and vertical directions, ensuring identical electromagnetic responses for both x-polarized and y-polarized incident waves. Below the patch is an F4B substrate with a thickness of $h_1 = 0.5$ mm ($\varepsilon_r = 2.65$ and $\tan\delta = 0.003$). Beneath the F4B substrate there is an air
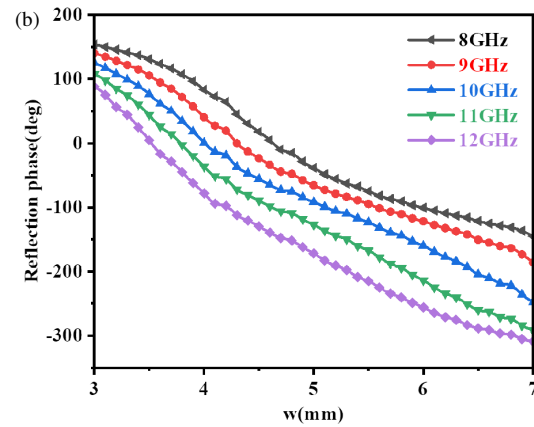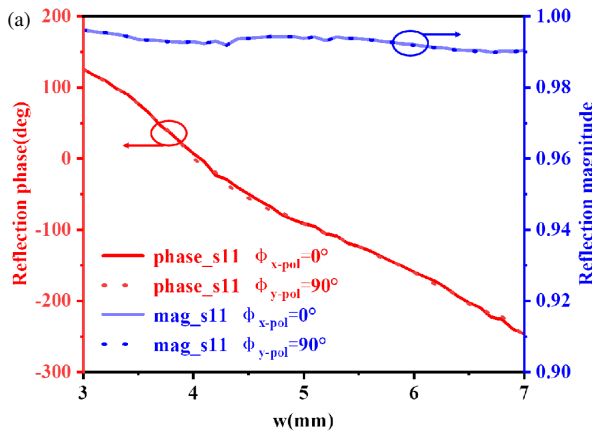
* Corresponding author: Lin Shao (linshao@sdust.edu.cn).
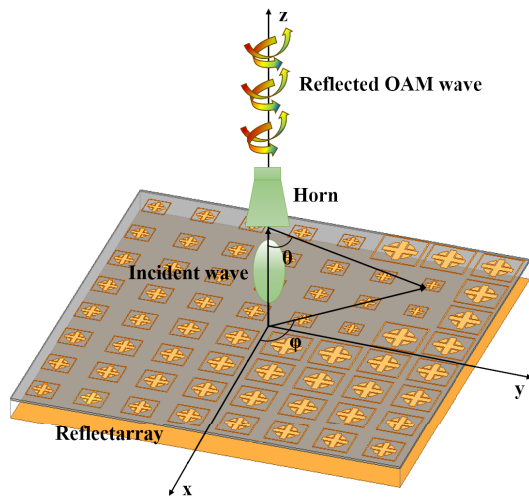
FIGURE 1. Schematic of the reflective metasurface generating OAM beams.
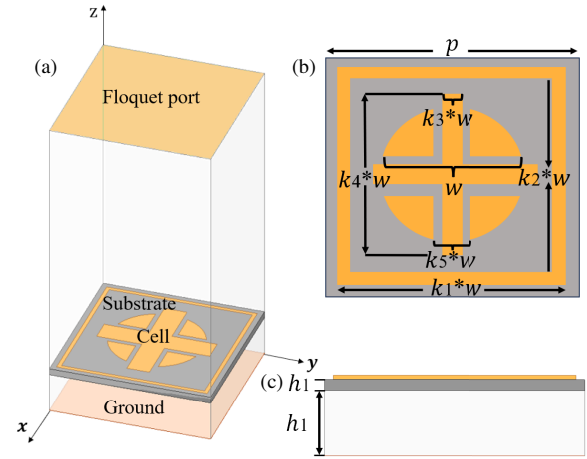
FIGURE 2. (a) Configuration, (b) top view and (c) side view of the unit cell.

FIGURE 3. (a) Phase shift and amplitude curves at 10 GHz. (b) Reflection phase at differnet frequency.

layer with a thickness of $h_2 = 5$ mm and at the bottom is a metal floor. After parameter optimization, the values obtained are $k_1 = 8$, $k_2 = 0.76$, $k_3 = 0.12$, $k_4 = 0.6$.

The unit is simulated and analyzed using electromagnetic simulation software with Floquet port boundary conditions. Fig. 3(a) illustrates the variations of reflection phase and S-parameters with w ranging from 3 to 7 mm, under both x-polarized and y-polarized incident waves at the central frequency of 10 GHz. As depicted in the figure, the reflection phase exhibits a continuous variation range of 374°, while the magnitude of the S-parameters shows minimal dependence on w. As parameter w varies, the curves of x-polarization and y-polarization overlap, indicating polarization insensitivity of the unit. This property enables the generation of dual-polarized vortex waves. Fig. 3(b) shows the trend of the reflection phase curves with w at different frequencies. Within the designed frequency band, the reflected phase curves demonstrate excellent parallelism and linearity with a shallow slope, suggesting low sensitivity of the reflected phase to variations in the unit dimension.

3. DESIGN OF METASURFACE ARRAY

The OAM reflective metasurface antenna is composed of two parts: a feed antenna and a reflective metasurface. In this paper, a standard horn antenna serves as the feed source. To generate vortex waves with $l = -1$, the proposed metasurface must produce the required helical phase distribution $\exp(-jl\varphi)$. When the phase center of the horn is positioned at vector location $\vec{r}_f$ and the metasurface composed of $M \times N$ units, the electric field at any position in space can be approximately represented as the superposition of the radiation fields from all units on the metasurface. This can be expressed approximately as [20]:

$$\vec{E}(\hat{u}) = \sum_{m=1}^{M} \sum_{n=1}^{N} F(\vec{r}_{mn} \cdot \vec{r}_f) A(\vec{r}_{mn} \cdot \hat{u}_0) A(\hat{u}_0 \cdot \hat{u})$$

$$\cdot \exp\left\{-jk_0 \left[|\vec{r}_{mn} - \vec{r}_f| + \vec{r}_{mn} \cdot \hat{u}\right] + j\phi_{mn}^c\right\} (1)$$

where A is the unit pattern function; F is the feed pattern function; $\vec{r}_{mn}$ and $\vec{r}_f$ are the position vector of the mnth unit and the feed respectively; $\hat{u}_0$ is the main beam direction.
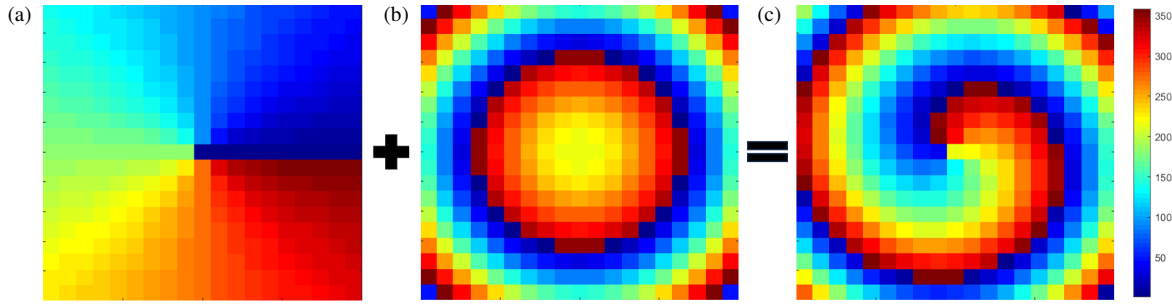
FIGURE 4. The necessary phase compensation for generating OAM beams: (a) the OAM desired phase, (b) the feed compensation phase, (c) the final compensation phase.
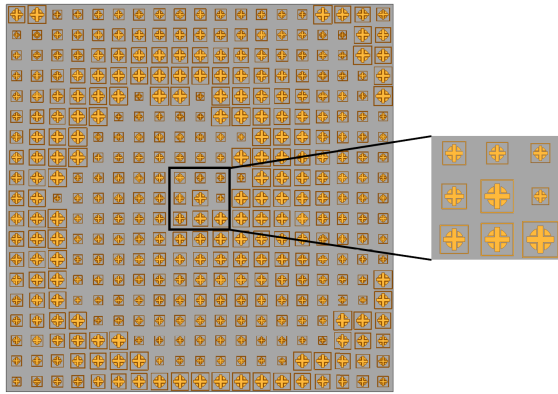
FIGURE 5. Schematic of the reflective metasurface.

To generate vortex waves with desired mode, the phase compensation for each unit should be [20]:

$$\phi_{mn}^c = k_0 \left[|\vec{r}_{mn} - \vec{r}_f| + \vec{r}_{mn} \cdot \hat{u}_0 \right] \pm l\varphi_{mn} \qquad (2)$$

where φ_{mn} is the azimuthal orientation of the mnth unit in metasurface, and l is the OAM mode number.

Based on above unit, a 19×19 metasurface array was designed at 10 GHz. The overall metasurface dimensions measure $228 \times 228 \text{ mm}^2$ ($7.6\lambda_0 \times 7.6\lambda_0$). The final phase compensation required was calculated in Fig. 4. Fig. 5 shows the corresponding metasurface configuration schematic.

The horn antenna is positioned 228 mm from the metasurface. Fig. 6 presents the simulated 2D far-field radiation patterns for x-polarized and y-polarized excitations respectively. The radiation patterns exhibit characteristic nulls at $\theta = 0°$ for both polarization states. For x-polarized excitation, the array achieves a peak gain of 20.6 dBi with a divergence angle of $6.03°$. Similarly, under y-polarized excitation, the array demonstrates comparable performance with a peak gain of 20.5 dBi and a divergence angle of $6.3°$.

Figure 7 presents the simulated near-field electric field amplitude distributions, which clearly exhibit hollow characteristics for both x-polarized and y-polarized excitations. The phase distributions in Fig. 8 demonstrate uniform counterclockwise 2π spiral rotations, confirming formation of helical wavefronts. These results are in excellent agreement with the characteristics of vortex waves with $l = -1$, verifying the successful generation of dual-polarized vortex waves.

For a quantitative analysis of the purity of the OAM modes, using Fourier analysis [21, 22] to decompose the individual OAM modes:

$$\psi(\varphi) = \sum_{l_i=-\infty}^{+\infty} A_l \exp(il\varphi) \qquad (3a)$$

$$A_l = \frac{1}{2\pi} \int_0^{2\pi} \psi(\varphi) e^{-jl\varphi} d\varphi \qquad (3b)$$

where A_l is the OAM spectrum, and $\psi(\varphi)$ is a function of the sampled field along the circumference of the z-axis. Here, the OAM modes from $l = -5$ to $l = 5$ are considered, and the energy spectrum weight of the OAM mode l is defined as follows [21]:

$$W = \frac{|A_l|}{\sum_{l'=-5}^5 |A_{l'}|} \qquad (4)$$

Figure 13 presents the mode purity analysis of the generated vortex waves under dual-polarization excitation. The results show that the designed mode $l = -1$ maintains dominance across the entire 8–12 GHz band. Under x-polarized excitation, the mode purity exceeds 72%, with an average of 76.4% over the bandwidth. Similarly, y-polarized excitation yields mode purity above 70% and an average of 76.2%.

The reflective metasurface is fabricated as shown in Fig. 9(a), with a planar area of 250 mm × 250 mm and an effective radiation area of 228 mm × 228 mm. The peripheral margin accommodates mounting holes supported by nylon pillars. The experimental setup schematic is illustrated in Fig. 9(b). Measurements are carried out in a microwave chamber, as shown in Fig. 9(c). The horn is positioned 228 mm from the metasurface, aligned with a receiving probe at a distance of 460 mm. The horn and probe are connected to a vector network analyzer 3672D. A 300 mm × 300 mm planar region was scanned with 10 mm resolution.

The measured electric field characteristics are presented in Figs. 10–12. Figs. 10 and 11 demonstrate the amplitude and phase distributions respectively, showing distinct doughnut-shaped amplitude patterns and complete 2π counterclockwise phase spirals for both polarizations, above characteristics consistent with $l = -1$ vortex waves. These experimental results agree well with the simulations shown in Figs. 7 and 8. Fig. 12 presents the measured 2D far-field radiation patterns.
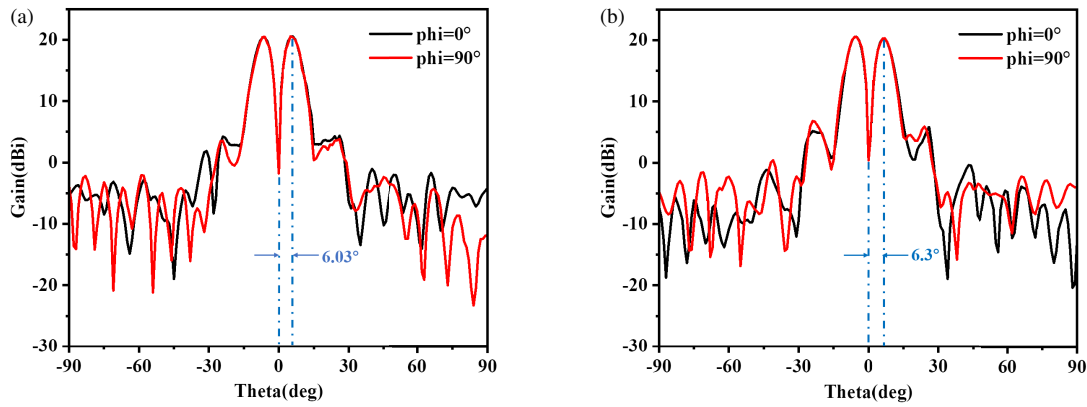
FIGURE 6. Simulated 2D far-field patterns for incident (a) x-polarized and (b) y-polarized waves.
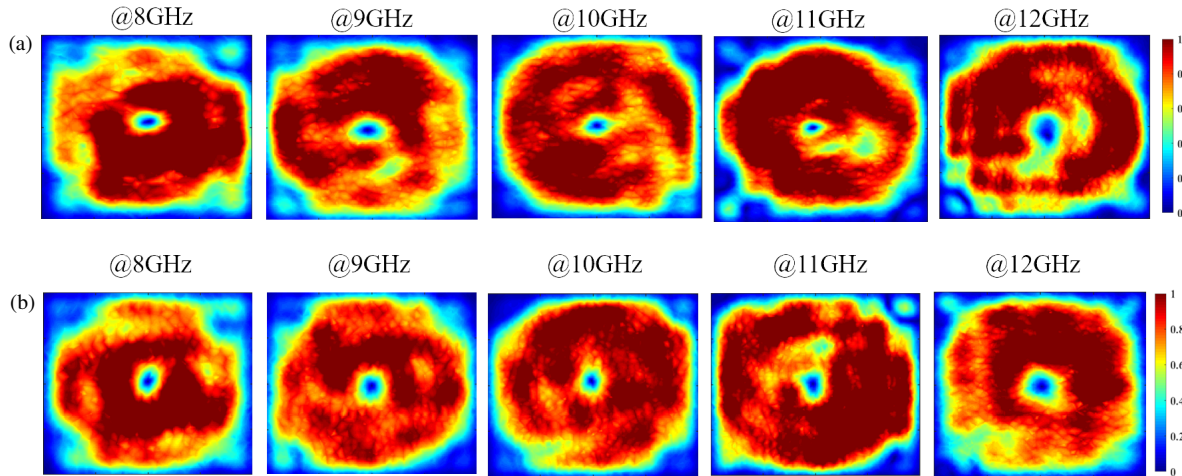
FIGURE 7. Simulated electric field amplitude distribution from 8 to 12 GHz in steps of 1 GHz under (a) x-polarized and (b) y-polarized incident waves excitations.
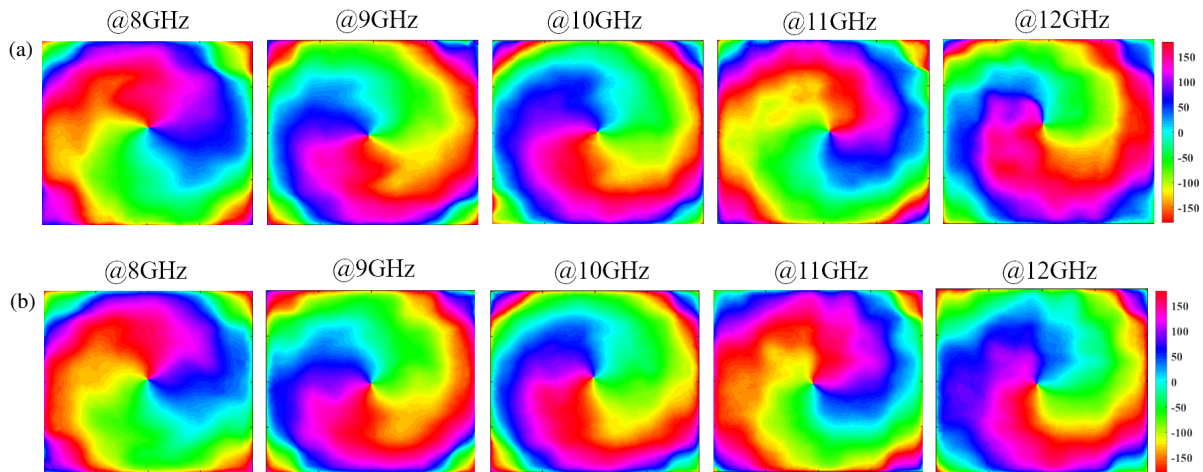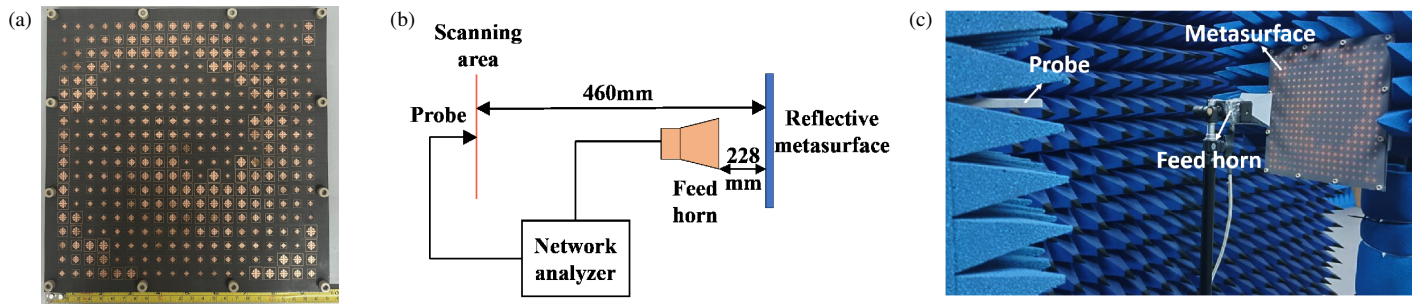

FIGURE 8. Simulated electric field phase distribution from 8 to 12 GHz in steps of 1 GHz under (a) x-polarized and (b) y-polarized incident waves excitations.

Under the incidence of x-polarized waves, the measured peak gain at 10 GHz reaches 20.3 dBi, with a beam divergence angle of approximately 6°, and the energy attains its minimum near $\theta = -2.7°$. For the incidence of y-polarized waves, the measured peak gain at 10 GHz is 20.3 dBi, with a beam diver-

gence angle about 6.2°, and the energy reaches its lowest point in the vicinity of $\theta = -2°$. Measured mode purity is shown in Fig. 13.

The measured results exhibit deviations from simulations due to several experimental factors. First, visual alignment
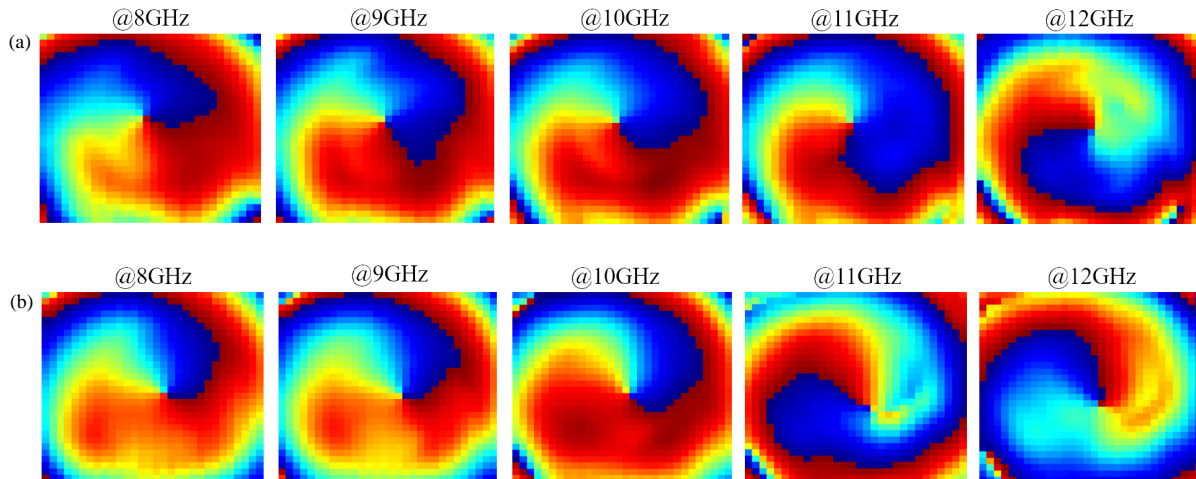
FIGURE 9. (a) The antenna prototype. (b) Experimental setup schematic of the near-field. (c) Near-field measurement in microwave chamber.
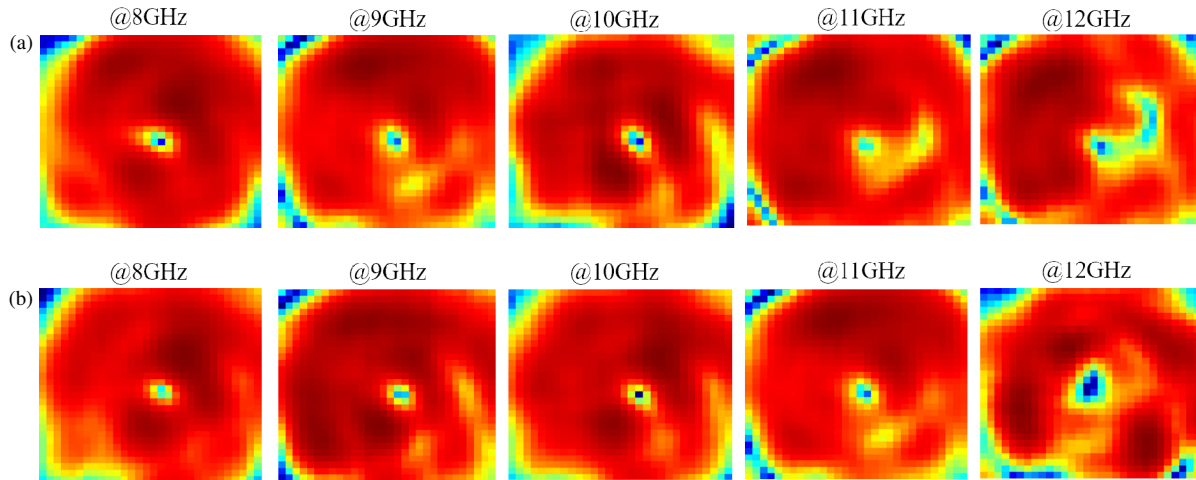
FIGURE 10. Measured electric field amplitude distribution from 8 to 12 GHz in steps of 1 GHz under (a) x-polarized and (b) y-polarized incident waves excitations.

FIGURE 11. Measured electric field phase distribution from 8 to 12 GHz in steps of 1 GHz under (a) x-polarized and (b) y-polarized incident waves excitations.

of the feed, probe, and metasurface introduces positional errors that shift the beam center and distort the phase distribution, leading to mode mixing and reduced purity. Second, surface irregularities in the array cause nonuniform radiation patterns, affecting both beam divergence and main lobe characteristics. Finally, fabrication tolerances in unit cell dimensions alter their phase modulation properties, further degrading the vortex wave quality. These cumulative effects account for the observed discrepancies between theoretical predictions and experimental measurements.

Table 1 shows the comparison between the proposed metasurface and other reported OAM antennas. Unlike the multi-
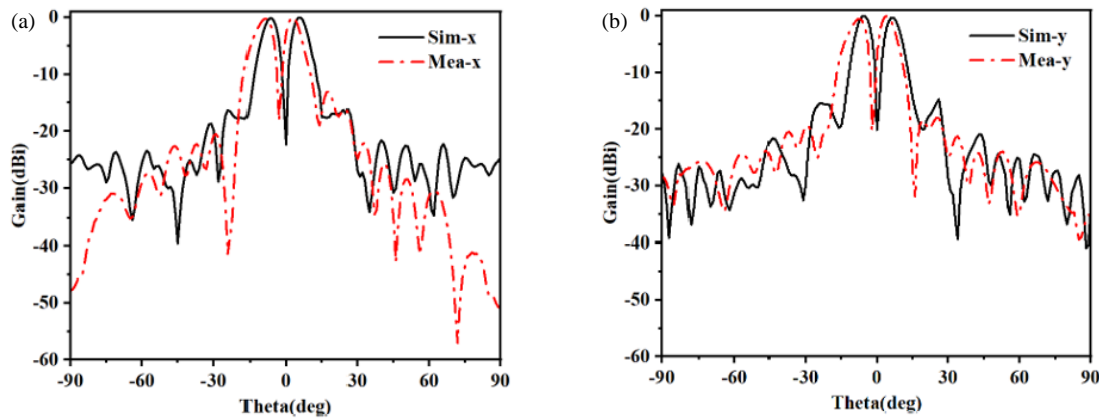
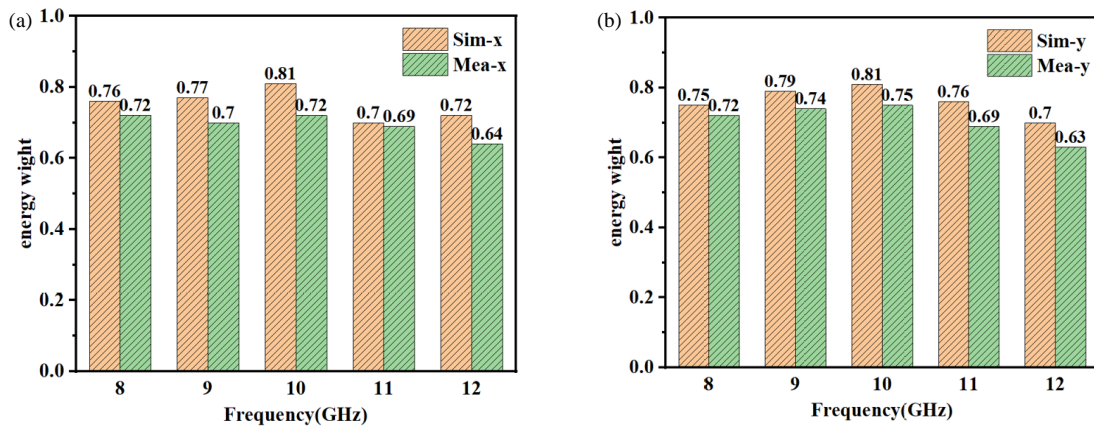FIGURE 12. Measured 2D far-field patterns for incident (a) x-polarized and (b) y-polarized waves.

FIGURE 13. Simulated and measured mode purity at 8–12 GHz for incident (a) x-polarized and (b) y-polarized.

TABLE 1. Comparison table with reported OAM antennas.

Ref.	Work Frequency	Unit Layer	Reflection Phase	Aperture Size (mm)	Metasurface Type	Peak Gain	Divergence Angle	OAM Purity
[23]	28–38 GHz	4	360°	$13.19\lambda_0$	dual-polarized	23.8 dBi	—	>= 72%
[24]	5.8 GHz	1	377°	$3.87\lambda_0$	dual-polarized	15.4 dBi	9°	>= 80%
[25]	26.5–40 GHz	1	473.6°	$8.89\lambda_0$	single-polarized	27.86 dBi	—	>= 70%
[26]	32 GHz	1	400°	$11.73\lambda_0$	single-polarized	21.5 dBi	4°	—
[27]	90–110 GHz	2	270°	$30\lambda_0$	single-polarized	17.5 dBi	—	>= 59%
Our Work	8–12 GHz	1	374°	$7.6\lambda_0$	dual-polarized	20.3 dBi	6°, 6.2°	>= 63%

layer structure [23], this design utilizes fewer layer to generation vortex waves. Compared to [24], this design has higher gain and narrower divergence angle. Furthermore, it maintains broadband operation across 8–12 GHz, outperforming the narrowband characteristics of [24] and [26]. In contrast to the single-polarized vortex beams generated by [25–27], this design generates dual-polarized vortex waves.

4. CONCLUSION

In conclusion, this work has successfully generated dual-polarized vortex waves at X-band. Under the conditions of the incidence of x-polarized and y-polarized waves, it can effectively generate vortex waves with $l = -1$ at the relative bandwidth of 40%. This metasurface features broadband and dual polarizations, which address the limitation of resonant reflective metasurfaces operating at single frequency. It enables polarization multiplexing and has potential applications in the field of vortex waves communications. Although it is currently optimized for low-order mode generation, the architecture shows potential for extension to higher-order modes through future optimization of unit cell geometry and array configuration. In the future, we will focus on generating vortex waves with superior performance and higher-order mode numbers.

PIER Letters

REFERENCES

[1] Yao, A. M. and M. J. Padgett, "Orbital angular momentum: Origins, behavior and applications," *Advances in Optics and Photonics*, Vol. 3, No. 2, 161–204, May 2011.

[2] Mohammadi, S. M., L. K. S. Daldorff, J. E. S. Bergman, R. L. Karlsson, B. Thide, K. Forozesh, T. D. Carozzi, and B. Isham, "Orbital angular momentum in radio — A system study," *IEEE Transactions on Antennas and Propagation*, Vol. 58, No. 2, 565–572, Feb. 2010.

[3] Lee, I., A. Sawant, and E. Choi, "High-directivity orbital angular momentum antenna for millimeter-wave wireless communications," *IEEE Transactions on Antennas and Propagation*, Vol. 69, No. 7, 4189–4194, Jul. 2021.

[4] Wang, Y., X. Sun, and L. Liu, "Millimeter-wave orbital angular momentum: Generation, detection, and applications: A review on millimeter wave orbital angular momentum antennas," *IEEE Microwave Magazine*, Vol. 25, No. 1, 37–57, Jan. 2024.

[5] Liu, D., L. Gui, Z. Zhang, H. Chen, G. Song, and T. Jiang, "Multiplexed OAM wave communication with two-OAM-mode antenna systems," *IEEE Access*, Vol. 7, 4160–4166, Dec. 2018.

[6] Tu, J., S. Gao, Z. Wang, Z. Liu, W. Li, C. Du, W. Liu, Z. Li, C. Yu, H. Tam, and C. Lu, "Bend-insensitive grapefruit-type holey ring-core fiber for weakly-coupled OAM mode division multiplexing transmission," *Journal of Lightwave Technology*, Vol. 38, No. 16, 4497–4503, Apr. 2020.

[7] Wang, Y., Y. Lu, C. Bao, W. Geng, Y. Fang, B. Mao, Z. Wang, Y.-G. Liu, H. Huang, Y. Ren, Z. Pan, and Y. Yue, "Hollow ring-core photonic crystal fiber with > 500 OAM modes over 360-nm communications bandwidth," *IEEE Access*, Vol. 9, 66 999–67 005, Apr. 2021.

[8] Wang, Y., W. Zhao, W. Geng, Y. Fang, C. Bao, Z. Wang, H. Zhang, Y. Ren, Z. Pan, and Y. Yue, "Air-core ring fiber guiding > 400 radially fundamental OAM modes across S+C+L bands," *IEEE Access*, Vol. 9, 75 617–75 625, May 2021.

[9] Mair, A., A. Vaziri, G. Weihs, and A. Zeilinger, "Entanglement of the orbital angular momentum states of photons," *Nature*, Vol. 412, No. 6844, 313–316, Jul. 2001.

[10] Zhang, Z., S. Zheng, Y. Chen, X. Jin, H. Chi, and X. Zhang, "The capacity gain of orbital angular momentum based multiple-input-multiple-output system," *Scientific Reports*, Vol. 6, No. 1, 25418, May 2016.

[11] Liang, Y., F. Zhang, and J. Gu, "Integratable quarter-wave plates enable one-way angular momentum conversion," *Scientific Reports*, Vol. 6, No. 7, 24959, Apr. 2016.

[12] Lin, M., Y. Gao, P. Liu, and J. Liu, "Theoretical analyses and design of circular array to generate orbital angular momentum," *IEEE Transactions on Antennas and Propagation*, Vol. 65, No. 7, 3510–3519, Jul. 2017.

[13] Meng, X., X. Chen, L. Yang, W. Xue, A. Zhang, W. E. I. Sha, and Q. Cheng, "Launcher of high-order Bessel vortex beam carrying orbital angular momentum by designing anisotropic holographic metasurface," *Applied Physics Letters*, Vol. 117, No. 24, 243503, Dec. 2020.

[14] Yu, S., L. Li, and G. Shi, "Dual-polarization and dual-mode orbital angular momentum radio vortex beam generated by using reflective metasurface," *Applied Physics Express*, Vol. 9, No. 8, 082202, Jul. 2016.

[15] Feng, Q., X. Kong, M. Shan, Y. Lin, L. Li, and T. J. Cui, "Multi-orbital-angular-momentum-mode vortex wave multiplexing and demultiplexing with shared-aperture reflective metasurfaces," *Physical Review Applied*, Vol. 17, No. 3, 034017, Mar. 2022.

[16] Liu, X., S. Li, C. He, Z. Li, G. Huang, and X. Cao, "Multiple orbital angular momentum beams with high-purity of transmission-coding metasurface," *Advanced Theory and Simulations*, Vol. 6, No. 4, 2200842, Feb. 2023.

[17] Xu, S.-Z., Y. Shen, Z. Wei, and S. Hu, "Low-profile circularly-polarized hybrid antenna for beam-switching and OAM mode-switching," *IEEE Transactions on Antennas and Propagation*, Vol. 73, No. 1, 33–43, Aug. 2024.

[18] Li, R.-C., M. Huang, and Y. Zou, "Broadband continuous integer- and fractional-order multimode OAM beam generator via a metasurface," *ACS Photonics*, Vol. 12, No. 2, 870–878, Jan. 2025.

[19] Pozar, D. M., "Bandwidth of reflectarrays," *Electronics Letters*, Vol. 39, No. 21, 1490–1491, Oct. 2003.

[20] Yu, S., L. Li, G. Shi, C. Zhu, X. Zhou, and Y. Shi, "Design, fabrication, and measurement of reflective metasurface for orbital angular momentum vortex wave in radio frequency domain," *Applied Physics Letters*, Vol. 108, No. 12, 121903, Mar. 2016.

[21] Yang, L.-J., S. Sun, and W. E. I. Sha, "Ultrawideband reflection-type metasurface for generating integer and fractional orbital angular momentum," *IEEE Transactions on Antennas and Propagation*, Vol. 68, No. 3, 2166–2175, Mar. 2020.

[22] Jack, B., M. J. Padgett, and S. Franke-Arnold, "Angular diffraction," *New Journal of Physics*, Vol. 10, No. 10, 103013, Oct. 2008.

[23] Ishfaq, M., X. Li, Z. Qi, W. Zhao, A. Aziz, L. Qiu, and S. Memon, "A transmissive metasurface generating wideband OAM vortex beam in the Ka-band," *IEEE Antennas and Wireless Propagation Letters*, Vol. 22, No. 8, 2007–2011, Aug. 2023.

[24] Huang, H.-F. and S.-N. Li, "High-efficiency planar reflectarray with small-size for OAM generation at microwave range," *IEEE Antennas and Wireless Propagation Letters*, Vol. 18, No. 3, 432–436, Mar. 2019.

[25] Fu, C., J. Zhao, F. Li, and H. Li, "A broadband vortex beam generator based on single-layer hybrid phase-turning metasurface," *Micromachines*, Vol. 14, No. 2, 465, Feb. 2023.

[26] Lei, X. Y. and Y. J. Cheng, "High-efficiency and high-polarization separation reflectarray element for OAM-folded antenna application," *IEEE Antennas and Wireless Propagation Letters*, Vol. 16, 1357–1360, Dec. 2016.

[27] Ali, A., M. Khalily, D. Serghiou, and R. Tafazolli, "Reflective metasurface with steered OAM beams for THz communications," *IEEE Access*, Vol. 11, 12 394–12 401, Feb. 2023.